
University of South Australia

The Library
www.library.unisa.edu.au

Educating Professionals, Creating and Applying Knowledge, Engaging our Communities

NOTICE: this is the author's version of a work that was accepted for publication in *Journal of Colloid and Interface Science*. Changes resulting from the publishing process, such as peer review, editing, corrections, structural formatting, and other quality control mechanisms may not be reflected in this document. Changes may have been made to this work since it was submitted for publication. A definitive version was subsequently published in *Journal of Colloid and Interface Science* 328(1):73–80
doi:10.1016/j.jcis.2008.08.063

Aggregate structure in kaolinite flocculation

Marek Zbik[a*], Roger St.C. Smart[b], Gayle E. Morris[a]
[a]*Ian Wark Research Institute, University of South Australia*
Mawson Lakes, South Australia 5095
[b]*ACeSSS (Applied Centre for Structural and Synchrotron Studies), University of South Australia*
Mawson Lakes, South Australia 5095

Abstract

Effective flocculation and dewatering of slurry streams containing clays (particularly kaolin and smectites which are often <200nm in lateral dimension) is becoming increasingly urgent. Release of water (often >75 wt%), for recycle and reduced make-up water consumption, from slurries in tailings streams and dam beds is usually slow and incomplete. To achieve fast separation of clays from water and minimization of retained water, individual particles need to be bound in the initial stages of thickening into large, high-density aggregates, which may sediment more rapidly with lower intra-aggregate water content. Quantitative cryo-SEM imaging shows that the structure of aggregates formed before flocculant addition has a determinative effect on these outcomes. Without flocculant addition, 3 stages occur in the mechanism of primary dewatering of kaolinite: initially separate particles and aggregates are dispersed a partially-gelled chain network forms linking particles edge-edge (EE) network; after an induction time, this network structure spontaneously rearranges from EE chains to stairstep face-face (FF) contacts building chains strings-like aggregates and finally compact FF aggregates. Densifying, compacting and dewatering the aggregates show high settling rates; during settling a network spanning the vessel with compressive strength in finally produced. The sponge-like structure with EE and FF oriented stairstep string-like aggregates limits slurry dewatering because the steric effect in the resulting partially-gelled structure is much more dominant than the electrostatic effects predicted by DLVO theory. The spontaneous rebuilding structure of aggregates from EE oriented chains to FF oriented compact aggregates has been observed but is slow. With flocculant addition, the internal structure and networking of the pre-aggregates is largely preserved but they are rapidly and effectively bound together by the bridging action of the flocculant(s). The statistical analysis from cryo-SEM imaging shows that there is a inverse correlation of intra-aggregate porosity (and void permeability) with Darcian permeability (and extent of dewatering) whereas there is a strong positive correlation of Darcian inter-aggregate permeability with settling and primary dewatering rate in function of pH in suspension.

Key Words: clays, flocculation, aggregate structure, dewatering, cryovitrification, SEM.

1. Introduction

Flocculation and dewatering of slurry streams containing significant proportions of clays is becoming increasingly urgent in view of the growing demand for high density disposal of mining slurries, tailings and other mineral wastes. Mine tailings are often disposed of as high water content slurries (e.g. >75 wt%) into tailing dams. Release of water, for recycle and reduced make-up water consumption, from these slurries in tailings streams and beds is usually slow and incomplete. Because clay particles are extremely small, generally <200 nm in lateral dimension, natural separation by sedimentation, governed by Stoke's Law, is very slow. For instance, clays as kaolinite largely determine the primary dewatering of tailings from coal, iron ore, heavy minerals and some base metal sulfide operations.

Primary dewatering processes include aggregate formation, bridging flocculation, settling rate and bed height (density) before compression. Aggregation is usually understood to be achieved by flocculation using long chain polymers but this process is not well understood. Our research, derived from the direct imaging and quantitative measurement of aggregate structures described in this paper, has shown that this understanding is incomplete and, in some respects misleading. The structure of aggregates formed before flocculant addition can be determinative of the sedimentation rate, the final bed density and the retained water after drainage.

It is well established in both theory and practice that changes in settling rates and solids density of tailings containing clays can be achieved in practice by changes in pH, dissolved cations and flocculant additions. Contemporary approaches to control clay suspension are based on colloid stability theory developed by Derjaguin & Landau (1941) and Verwey & Overbeek (1948) known as the DVLO theory where competing electrostatic and van der Waals forces generally decide whether particular colloid clay suspensions will be stabilised (in sol form) or coagulated (in gel form). On this basis, Hogg (2000) described opportunities for control of floc characteristics by physical displacement between particles, chemical changes in pore electrolyte, and introduction of new mineral phases into the system. All of these manipulations may collapse the electrical double layer which will lower the electrokinetic potential and allow particles close enough for van der Waals forces to bond particles into larger aggregates which significantly increase settling rates. To be successful, these manipulations require initial dispersion of the clay particles in suspension.

Based on Hogg's review and our results, the initial proposition can be put forward that, to achieve fast separation of clays from water and minimisation of retained water, individual

particles need to be bound into high-density, low-internal-porosity aggregates before flocculant addition, which may then sediment more rapidly with lower intra-aggregate water content. To build these aggregates, specific structures must be developed in the clay suspension in the initial stages of thickening. This pre-flocculant structure is determined by the mineral surface structure and chemistry together with the solution chemistry. Our previous experience with SEM/AFM studies on clay mineral morphology and texture has played an important role in understanding platelet shape, aspect ratio, roughness of the basal planes of platelets and the role of floc porosity in structure forming phenomena (Zbik & Smart 1998, 1999; Zbik, Self and Smart, 1999). The second part of the proposition is that, with flocculant addition, the internal structure and networking of the pre-aggregates is largely preserved but they are rapidly and effectively bound together by the bridging action of the flocculant(s) to produce larger, linked aggregates that sediment fast. Provided that the flocculant is chosen to give effective adsorption (charge) and bridging (length, charge density), it is the pre-flocculant structure that requires optimization for most effective water exclusion.

The evidential basis of this proposition comes from the development of a very useful technique involving cryo-vitrification of slurry structure followed by partial sublimation of vitrified water and cold stage SEM to image low density floc structures directly. This has enabled the measurement of porosity and the calculation of permeability from the SEM images using STIMAN image analysis. The STIMAN quantitative image analysis software was developed in Professor Sokolov's group at Moscow State University (Sergeev et al., 1983a,b) and adapted for application to clay aggregate systems.

2. Materials and methods

2.1. Clay sample studied

A Commercial Minerals Ltd. white kaolinite CML K15GM produced at Adelaide, South Australia from CML Birdwood quarry, surface area 19.7 m^2/g was used. XRD description of this sample has been given in Frost et al (2002), SEM characterization of the mineral particles is illustrated in Fig. 1. The zeta potential of this material is presented in Figure 2. They are generally roughly hexagonal platelets <300nm with high aspect ratio (Zbik and Smart, 1998, 1999) and edge/face ratio ~0.25. This kaolinite has a relatively high measured GP in the range 10-12 wt%.

A variety of commercially available polyacrylamide flocculants with different charges and molecular weights, widely used throughout the mining industry for tailings treatment, was

used in the study. For the series of experiments presented in this paper, only the anionic Cytec Superfloc A130, with molecular weight ~15 x 10^6Da and moderate charge is reported. The flocculant dosages ranged from 0 to 0.029 mg/m^2 (~ 600 g/tonne).

2.2. SEM analysis

In the cryovitrification SEM studies using STIMAN analysis, the sample is taken by a large-aperture (>2 mm) pipette directly from the flocculating system at chosen times and depths, e.g. immediately after dispersion, from the top, middle or bottom of the sedimenting column or from the top of the settled bed. The sample is immediately plunged into a Dewar of liquid propane, cooled by liquid nitrogen, which reduces the temperature at >1000 ^{o}C/min freezing the water without allowing crystallization, i.e. vitrifying (Battersby et al., 1994). Vitrified samples are placed onto the liquid nitrogen-cooled specimen stage of the field emission scanning electron microscope Philips XL30 FESEM with Oxford CT 1500HF Cryo stage. The Sample is fractured under vacuum and a small amount of vitrified H_2O sublimed off by raising the stage temperature to -90 ^{o}C (for period ~30 second) then lowering back to ~-180 ^{o}C. This technique exposes the structure of the snap-frozen aggregates proud of the surface of the vitrified water greatly improving imaging and quantitative image analysis. Finally, a 3 nm gold and palladium, high resolution coating is sputtered on to the exposed surface to increase conductivity before SEM imaging. Typical micrograph from aqueous kaolinite low solid suspension has been shown in Fig. 3 where bright kaolinite platelets are protruding from dark vitrified water ice, description of the Birdwood kaolinite investigation and comparison against Georgia kaolinite using crio-SEM has been detailed in Zbik (2006).

2.3. Settling rates and permeability/dewatering

Conventional settling rate column tests have been conducted in cylinders as described in Taylor et al. (2003). Examples of data for kaolinite tests at different pH are shown in Figure 4. The flocculant dosage may appear to be large but, to put this in context for a tailings (5 m2/g) with 60% kaolin, a dosage of 0.029 mg/m2 corresponds to ~45 g/tonne which is within industry norms. In these examples of results, the fastest (initial) settling rate and the highest bed density are found at pH 8. The settling rate and bed height at pH 10 (not shown) lie between pH 8 and pH6. It is also clear that the settling height curves are continuously curved

(Figure 4). That is, there is no region on the settling height curves that can be ascribed to free or unhindered settling. This suggests that the clays in suspension have formed an interacting network that may inhibit settling.

To consider this type of data in relation to permeability and dewatering, Darcian theory is usually the starting point. In dewatering of a suspension, two regions of behaviour exist – at high solids, a particle network is formed spanning the vessel with compressive strength; at low solids, inter-particle contact occurs but a spanning network is not formed. The transition is the gel point ϕg (Buscall and White, 1987). Darcian permeability $k(\phi)$ represents the inter-particle dewatering and is measured by the hindered settling function $R(\phi)$ which takes into account the hydrodynamic interactions between particles increasing drag during the first stage of settling.

Below the GP, in initial settling before compression, the two relevant equations are (Kretser, Usher and Scales, 2002):

$$R(\phi) = \Delta\rho\, g\, (1- \phi 0)2/Si \qquad (1)$$

where $\Delta\rho$ is the solid-liquid density difference, $\phi 0$ is the initial solids volume fraction and Si is the initial settling rate and

$$k(\phi) = \eta/ R(\phi)\, .\, (1- \phi)/ \phi \qquad (2)$$

where η is the viscosity of the solid-solution at the volume fraction ϕ.

Hence we can estimate the Darcian inter-particle permeability $k(\phi)$ below the GP from measurement of the initial settling rate and the viscosity of the suspension. This will allow comparison with inter- and intra-aggregate permeability estimated from crio-SEM image analysis.

3. Results and discussion

The electron-microscopic study of the clay fraction (<2 μm) of studied kaolinite reveals that sample consists of pseudo hexagonal euhedral crystals with diameters down to ~50 nm (Fig. 1). The crystals are typically thin and flexible plates. AFM investigations of this kaolinite (not show here) show that crystals are on average 160 nm in diameter and about 13 nm thick giving the aspect ratio values ~12. A few grape shaped anatase aggregates and a few tubular halloysite particles were also observed.

The electrokinetic (zeta) potential measured for in kaolinite sample shown in Fig. 2. displays negative values of Zeta potential with pH-dependent profile due to OH^- groups occupied platelets edges in high pH. However pH dependence is low in compare to other high

crystalline kaolinites and small zeta potential variances profile suggesting dominance of the basal planes. This may be an effect of platelets high aspect ratio where edges area contribution to the surface area is much smaller in comparison with better crystalline kaolinite.

3.1. Kaolinite aggregation: no flocculant

Figure 5 superimposes SEM images of the aggregate structure from the different stages of settling for 4 wt% Birdwood kaolinite suspension in pH 8 & 0.01 M NaCl without flocculant addition. There are three significant stages (a, b, c) in the aggregate forms during this process.

Each stage is illustrated in more detail in Figures 6a, b and c. In Fig. 6a, taken in the earliest stage of dispersion possible before there is any apparent settling, the structures already show edge-edge (EE) and edge-face (EF) inter-particle associations but these are open, loose and easily disrupted. These particles and chained aggregates still appear to be flocculated but dispersed accordingly to Van Olphen (1963) model. In this model, particles and EE chain associations build spanned network across vessel and resists sedimentation. After some induction time (which vary with solid loading and electrolyte characteristics), settling has started (Fig. 6b), the solids density in the settling region is still below the GP (~0.6) but the aggregates are now arranged into chain-like structures of stairstep face-face (FF) associations apparently quite strongly adherent. Similar stairstep chain aggregate building cardhouse-like structures have been observed previously by O'Brien (1970, 1971) using freeze-drying techniques but this technique can alter structure during drying. Individual platelets in FF stepped aggregate appear to slide across each other forcing chain aggregate to contracts. This contraction leads to fragmentation of previously spanned network and formation of individual flocks. The images suggest that the solids density within each flock chain is likely to be well above the GP. Nevertheless, this structure remains largely suspended apparently because it does not bridge the vessel and confer a compressive resistance. Settling rate in this stage is high and can exceed those expected by Stoke's Law from relatively large particles >20μm. This dramatic increase of settling rate is probably enhanced by observed chain-like aggregate spontaneous contraction. Mechanism of this spontaneous chain aggregate contraction observed in crio-SEM micrographs is still unknown. The platelets sliding across each other, despite their negative zeta potential, suggesting hydrophobic or van der Waal's forces are involve at these very close distances of approach.

The first two stages where sponge-like chain structure with EE oriented particles, after the

initial flocculated but dispersed stage, likely limits slurry dewatering because the steric effect in the resulting partially-gelled structure is much more dominant than the electrostatic effects predicted by DLVO theory. As particles slide across each other in the second stage, the particle mutual orientation changes from EE to stairstep FF. The previously extended network spontaneously contracts, and when the solid volume fraction is low, the continuous network breaks apart forming aggregates and aggregate associations as flocs which are able to freely settle. These dense structures settle at increased rate, give lower bed density and retain less water after drainage.

Finally, contraction produce smaller but compact aggregates like seen in Fig.6c. In this figure major rearrangement of the aggregate structure from EE and EF through FF stairstep to FF compact aggregates has occurred somewhere in the transition to rapid settling, the overall GP, compressive resistance and bed density.

Addition of Ca^{2+} ions to the kaolin suspension shows a significant aggregation consisting of both short chain irregular shape aggregates and individual particles. In Fig. 7A(a) kaolinite is disperse in 0.01 M NaCl solution and chain aggregates are oriented in EE pattern. In Fig. 7A(b) the same kaolinite sample is suspended in 0.00025 M $CaCl_2$ solution. In this micrograph with Ca^{2+} cations present, aggregates are 2-5 μm in dimension look secondary and consists of individual particles aggregated mostly in FE orientation. These aggregates have often butterfly shape where a number of platelets are connected along one of the edges or stack to the face of another platelet. Individual particles (0.3 μm long) are also present. Neither, aggregates nor individual particles are connected into the spanning network. Intra-aggregate pores calculated from SEM images using STIMAN are small (0.54 μm) and space between aggregates is up to 17 μm and broadly distributed. Low average pore hydraulic diameter, within aggregates influences the filtration coefficient which is very low, similarly to other suspension samples without flocculant addition. But as the diagram in Fig. 7B shows the permeability index of the Ca^{2+} suspension is an order of magnitude larger than what present in Na^{+} electrolyte solution. This can be an effect of the different aggregate structure where in Ca^{2+} solution voids inside aggregates are larger due the rather FE particle orientation which differ from nano-size voids in long EE oriented and stairstep aggregates in the Na^{+} electrolyte.

3.2. Effect of flocculant addition on structure

Addition of anionic flocculant did not changed particle mutual orientation but only causes bonding of closer and denser micro-aggregates, as seen on micrographs studied in suspension 6 pH. Fig. 7A© shows similar chain aggregates EE oriented like in not flocculated sample Fig. 7A(a) but chains now are cross linked to other similar aggregates make flocks in suspension larger. In other words, addition of flocculant to kaolinite suspension freeze pre-existing particle mutual orientation but not changes it. In presence of Ca^{2+} ions shown in Fig. 7A(d) also prevailing FE orientation has been preserved and aggregates were cross linked making flocks larger than predeceasing aggregates but not denser. Pore space inside the micro-aggregates is larger with Na^{+} ions presence and much smaller with Ca^{2+} based electrolyte. This difference reflects different mutual orientation within aggregates in both systems.

For the same 4 wt% kaolinite now in 0.01 M NaCl at pH 8, the addition of 0.029 mg/m2 of flocculant A130 to the initial dispersion, in examples we have examined to date, results in aggregate structures like those in Figure 8. They appear to be closely similar to those from the first and second stages of loose EE structures and EE chain formation without flocculant (Figs. 6a, b). The flocculant appears to lock this structure before transition to the denser FF fourth stage structures. Whilst this may not be universally true for other systems, it is consistent with the action of the flocculant bridging the existing aggregate structures without significantly altering their internal or inter-particle structure. The effect of the flocculant is then primarily to make larger, locked inter-aggregate structure that should sediment faster at least until the GP is reached. However, the intra-aggregate water trapped in the initial structures is probably retained in this process if the denser FF aggregates do not have time to form.

3.3. Effect of pH on structure

In studied Birdwood kaolinite 4 wt% suspension in ranges of pH's the differences in microstructure defined by mutual particle arrangement was small. In lower pH's structure has high void ratio where individual platelets are largely EE orientated in chained aggregates. Chain-ggregates are few μm long but only single kaolinite platelets in thickness. When the pH is increased, the long chained aggregates appear be thicker and mostly in starsteps FF particle orientation. In crio-SEM images such chained aggregates build cellular spanned network

(within frame). EF orientation observed in other kaolinite samples (Zbik 2006) are rare in studied Birdwood kaolinite.

Differences in the aggregate structures in the flocculated material, with flocculant added, as a function of pH are also consistent with the behaviour of the flocculant as the net charge changes. This can be seen in the sequence of samples from the same system at different starting pH values of 4, 6, 8 and 10. The samples are taken from close to the top of the sedimented bed, i.e. the final stages of flocculation above the GP. At pH 4 (Figure 8a), the aggregates appear to be largely separate, loose, disordered associations consisting of EE, EF and FF structures but they are apparently not adherent. This is consistent with the relatively low or neutral surface charge on the adsorbed polymer at this pH, adsorbed flat to the surface and unable to extend between aggregates and inhibiting the settling rate. At pH 6 (Figure 8b), a very different linked, porous aggregate structure is found with much more EE chain development but still some EF disorder. The structure is more compact than pH 4 but appears likely to be still relatively flexible. At pH 8 (Figure 8c), there is more densification near the top of the bed with EF and now FF compaction clearly evident. The structure is still porous on the meso-pore scale but the intra-aggregate micro-pores appear smaller. At pH 10 (Figure 8d), the structure is quite similar to pH 8 but may have started to open out again with an apparent increase in disorder of the chains likely due to the increasing negative nett charge on the polymer. EE and FF stacking dominate the pH 10 structure but the region at lower right in Fig. 8d illustrates this increasing disorder as the settling rate and bed density decrease from those at pH 8.

3.4. Porosity-permeability-dewatering correlations

It is now possible to examine the crio-SEM micrographs of aggregate porosity and permeability in these different pH systems. Fig. 9 summarises the STIMAN porosity analysis with comparison to the settling rates for each pH system. In this analysis, closed porosity is calculated from void (dark areas in micrographs) regions completely bounded by (light areas in micrographs) particles and open porosity is calculated from void regions that are not completely bounded excluding those open to the edges of the micrograph region. The micrograph series of 5 magnifications across 500-8000x were used to calculate these micro-structural parameters.

The data shows that, at pH 8, the highest settling rate corresponds to the lowest total porosity and, importantly, the lowest open porosity. Closed porosity is similar across pH 6, 8

and 10. Comparison of the permeability calculated from the Darcian inter-aggregate theory as in equation (2) above, using the measured hindered settling rate and viscosity of the sample, with intra-aggregate permeabilities calculated from the STIMAN analysis has been show in Fig. 10. Note that the permeability scale is logarithmic so that the differences between indices and between pH values are larger in absolute numbers. This analysis shows that the Darcian inter-aggregate permeability is similar in value to STIMAN calculated permeability for most of pH range except pH 8. In pH 8 Darcian permeability is highest which corresponds with lowest porosity especially open porosity (inter-aggregate) calculated from crio-SEM micrographs with large voids channels within intra-aggregate porosity and highest settling rate. This likely to be most closely related to primary dewatering and bed density, has a maximum at pH 8. However, the intra-aggregate permeability, likely to be most representative of the trapped residual water in the settled bed, has a shallow minimum at pH 8. This permeability is particularly low for water trapped in pores <5 μm. The aggregates at pH 4 (Fig. 6a) apparently contain very little void space at this scale.

The porosity factor has a strong influence on floc permeability. More porous flocs with less density and with low initial settling rate have higher permeability than compacted low porosity dense flocs that settle fast. This view is supported by correlating the maximum settling rate and minimum (total and open) intra-aggregate porosity with minimum intra-aggregate permeability calculated in STIMAN. Graphs of partial void contributions in STIMAN estimates (Figure 11) also show that it is not total porosity that counts in permeability but the abundance of larger intra-aggregate voids that plays the crucial role. At pH 4, the largest pores are ~5 μm compared with the largest pores at pH 8 of 28 μm. The larger filtration at pH 10 is governed by channels up to 40 μm in diameter.

4. Conclusions

CM kaolinite from Birdwood consists of pseudohexagonal platelets down to 50-200 nm in diameter with thickness 160 nm and aspect ratio ~12. In Na^+ based electrolyte and in range pH's builds a very high void ratio structure where individual platelets are largely EE orientated or separate chained aggregates. Chain-ggregates are few μm long but only single kaolinite platelet in thickness. When the pH is increased to 8, the long chained aggregates appear be thicker and mostly in starsteps FF particle orientation. EF orientation is rare. In Ca^{2+} based electrolyte, the aggregate shape is significantly different. Aggregates are less

elongated and rather irregular with all possible platelet contact orientations with EF in preference.

Addition of flocculant, preserves the preexistant micro-structure by bridging the existing aggregate structures without significantly altering their internal or inter-particle structure. The effect of the flocculant is then primarily to cross linked preexistant aggregates, make them larger but locked up intra-aggregate preexistant structure. This effect make aggregates closer which fragments the spanned network and allow suspension to sediment faster at least until the GP is reached again. This lowers the total porosity in all solution conditions studied and triggers a larger filtration coefficient, which is highest in Ca-based electrolyte inspite of a moderate total porosity value. Once again large numbers of high hydraulic radii pores have a deciding influence on the inter-aggregate filtration coefficient.

The effectiveness of water release from within aggregates of the network skeleton depends on permeability of the system and can be characterised from both settling rates and porosity measurement. After network fragmentation and floc formation, the suspension consists of two different structural environments in the system which differ in permeability values:

- denser flocs consisting of aggregates with their internal permeability calculated from crio-SEM micrographs.
- solution space between flocs and aggregates where permeability is characterised by the Darcy formula based on hindered settling rate.

Knowing that addition of flloculant has little influence on intra-aggregate structure but the large voids within aggregates plays crucial role in permeability it is to restructuring of the aggregates before flocculant addition to improve settling rate and final solids density.

ACKNOWLEDGEMENTS

The author would like to acknowledge the staff at Adelaide Microscopy, the University of Adelaide. Research in this project has been supported by RioTinto (Australia) and the Australian Research Council Linkage Grant Program. We are particularly grateful to Dr. Mark Coghill for many valuable discussions of the results and to Dr. Ray Shaw for his continued support and permission to report the results.

REFERENCES

Battersby, B.J., Sharp, J.C.W., Webb, R.I., Barnes, G.T. 1994, Vitrification of aqueous suspensions from a controlled environment for electron microscopy: an improved plunge-cooling device. Microscopy M1192 p. 914.

De Kretser, R., Usher, S., Scales, P. 2002, Full de-waterability characterization of suspensions from tree settling to sediment compression. In "Solid Liquid Separations III", United Engineering Foundation Conference, Davos, Switzerland: Submited to Int. J. Min. Process.

Derjaguin, B.V. Landau, L.D., 1941, Theory of Stability of Highly Charged Lyophobic Sols and Adhesion of Highly Charged Particles in Solutions of Electrolytes, *Acta Physicochimica URSS.* 14 633-652.

Hogg, R., 2000, Flocculation and dewatering. *Int. J. Miner. Process.* 58. p. 223-236.

Kotlyar, L.S., Sparks, B.D, Lepage, Y., Woods, J.R., 1998, Effect of particle size on the flocculation behaviour of ultra-fine clay in salt solutions, *Clay Minerals* 33 103-107.

O'Brien, N.R., 1970, Freeze Drying Technique in the Study of the Fabric of Moist Clay Sediment, *Journal of Electron Microscopy* 19 277.

O'Brien, N.R., 1971, Fabric of kaolinite and illite floccules, *Clays and Clay Minerals* 19 353-359.

Schoonheydt, R.A., 2002, Smectite-type clay minerals as nanomaterials. *Clays and Clay Minerals.* 50, 411-420.

Sergeev, Y.M., Spivak, G.V., Sasov, A.Y., Osipov, V.I., Sokolov, V.N., Rau, E.I., 1983a, Quantitative morphological analysis in a SEM-microcomputer system-I. Quantitative shape analysis of single objects. *Journal of Microscopy,* 135, p. 1-12.

Sergeev, Y.M., Spivak, G.V., Sasov, A.Y., Osipov, V.I., Sokolov, V.N., Rau, E.I., 1983b, Quantitative morphological analysis in a SEM-microcomputer system-II. Morphological analysis of complex SEM images. *Journal Microscopy*, Vol. 135, Pt 1. p. 13-24.

Verwey, E.J.W., Overbeek, J.Th.G., 1948, The Theory of Stability of Lyophobic Colloids, Elsevier, Amsterdam, Netherlands.

Zbik M., Smart R.St.C., 1998, Nano-morphology of kaolinites: comparative SEM and AFM studies. *Clays and Clay Minerals.* 46 153-160.

Zbik M., Smart, R.St.C., 1999, Atomic force microscopy in the aspect ratio estimation of colloidal kaolinite. in "Clays For Our Future" (Eds. H. Kodama, A.R. Mermut and J.K. Torrance), Proceedings of the 11th International Clay Conference, Publ. ICC97 Ottawa, Canada, p. 361-366.

Zbik, M., Self, P., Smart, R.St.C., 1999, Coagulation edge to edge contacts between clay particles in dilute aqueous suspension; the major obstacle of fine clay waste dewatering. Abstracts EUROCLAY 1999, Krakow, Poland, p. 149.

Frost, R.L. Van Der Gaast, S.J. Żbik, M. Kloprogge, J.T. Paroz, G.N. Birdwood kaolinite: a highly ordered kaolinite that is difficult to intercalate-an XRD, SEM and Raman spectroscopic study. Applied Clay Science. 20 (2002) 177-187.

Żbik, M. (2006) Micro-Structural Explanation for Differences in Gelation Properties of Kaolinites from Birdwood (S. Australia) and Georgia (U.S.A). *Clay Csience, 12 (Suppl. 2)*, 31-36, 2006

Figure captions

Fig. 1. High resolution SEM micrographs of the clay fraction of kaolinite K15GM at two magnifications.

Fig. 2. Zeta potential of kaolinite K15GM measured on Rank Brothers microelectrophoresis instrument.

Fig. 3 Crio-SEM micrograph shows the cellular structure in spanned network of chained kaolinite aggregates in the 4 wt% kaolinite aqueous suspension.

Fig. 4. Settling curves from sediment height as a function of time for 4 wt% kaolinite in 0.01 M NaCl with 0.029 mg/m2 A130 flocculant added at different pH 4, 6, 8.

Fig. 5. Settling curve and aggregate structures for 4 wt% Birdwood kaolinite suspension in pH 8 and 0.01 M NaCl or flocculant addition.

Fig. 6. Enlarged micrographs from Figure 5 corresponding to: (a) first sample-dispersed stage; (b) third stage-pseudo-gelled chain structures; and (c) fourth stage FF-compacted structures.

Fig. 7. SEM micrographs from kaolinite suspension without flloculant present (a & b) and with after flocculant (A130) addition (c & d) with Na^+ and Ca^{2+} ionic solution adjusted to pH 6 sampled near the top of the sediment bed: a, Na; b, Ca; c, Na + A130; d, Ca + A130.

Fig. 8. SEM micrographs from flocculated kaolinite samples with adjustment of pH 8 but sampled near the top of the sediment bed: a, pH 4; b, pH 6; c, pH 8; d, pH 10.

Fig. 9. Porosity analysis from the crio-SEM-STIMAN micrographs, from flocculated kaolinite samples prepared at pH 4, 6, 8, 10 combining images across.

Fig. 10. Permeability values from measured Darcian parameters in equation (2) compared with permeability indices calculated from crio-SEM-STIMAN image analysis from flocculated kaolinite samples.

Fig. 11. Histograms of partial pore contributions to total porosity from pH 4 (upper) and pH 8 (lower) micrographs from flocculated kaolinite samples.

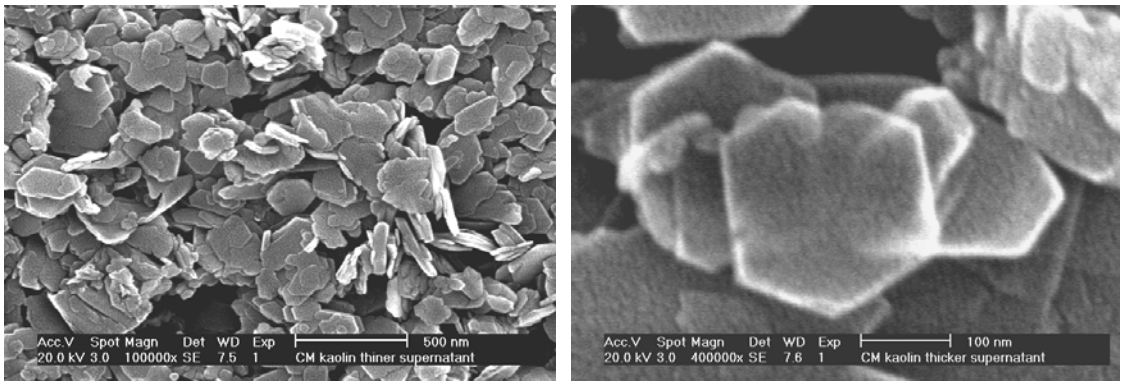


Fig. 1. High resolution SEM micrographs of the clay fraction of kaolinite K15GM at two magnifications.

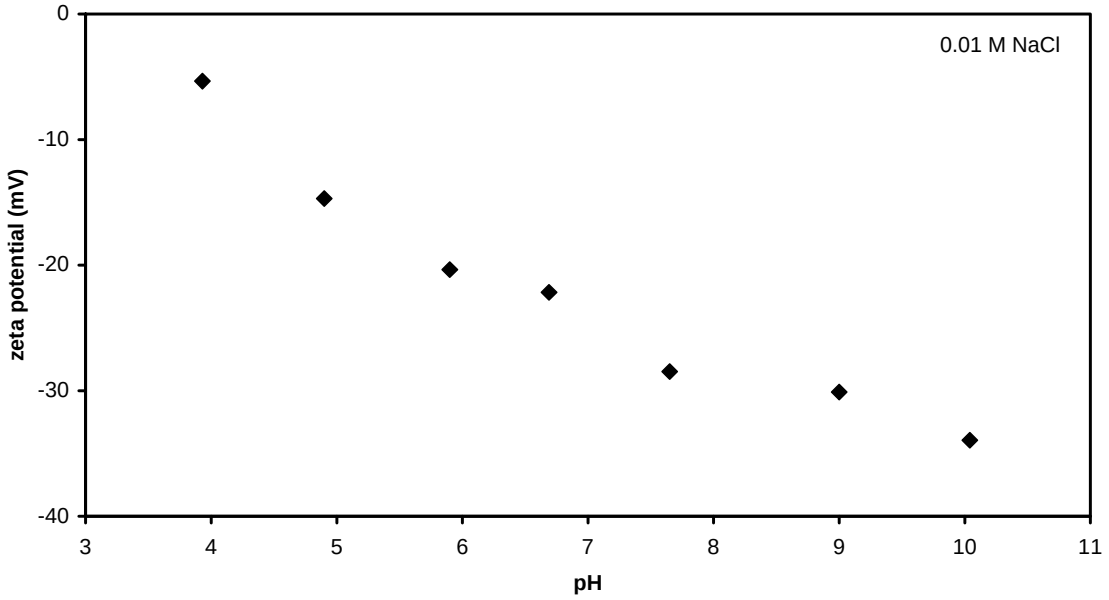


Fig. 2. Zeta potential of kaolinite K15GM measured on Rank Brothers microelectrophoresis instrument.

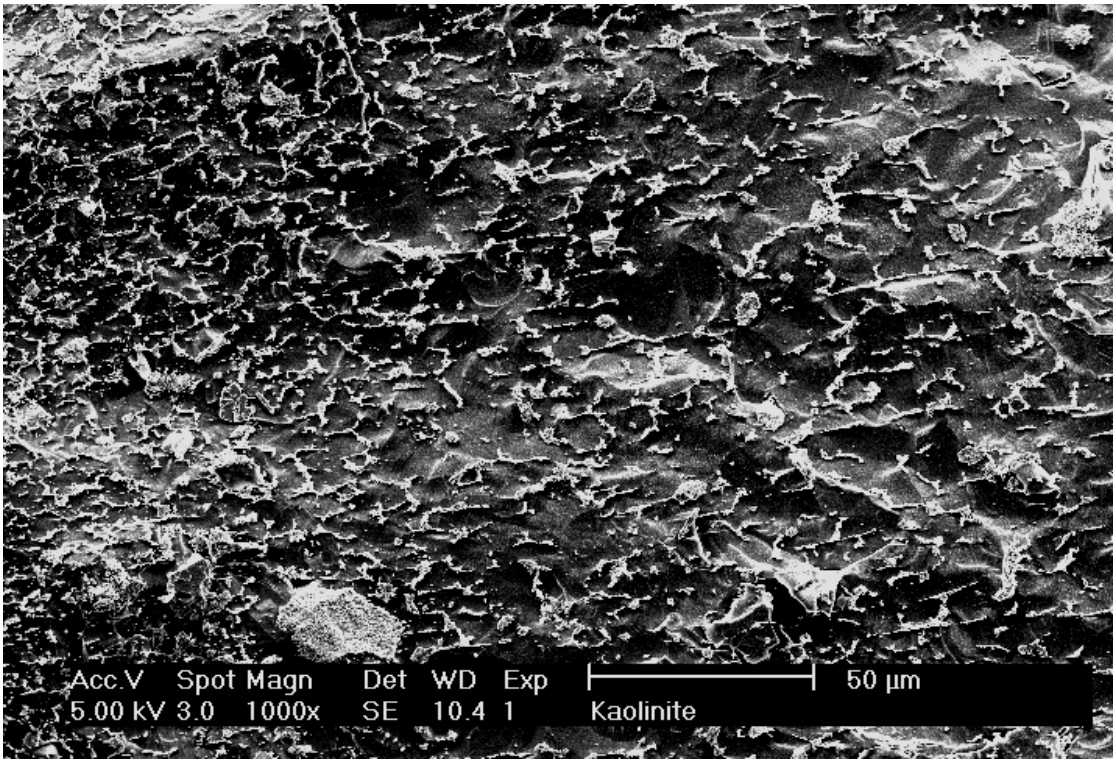


Fig. 3 Crio-SEM micrograph shows the cellular structure in spanned network of chained kaolinite aggregates in the 4 wt% kaolinite aqueous suspension

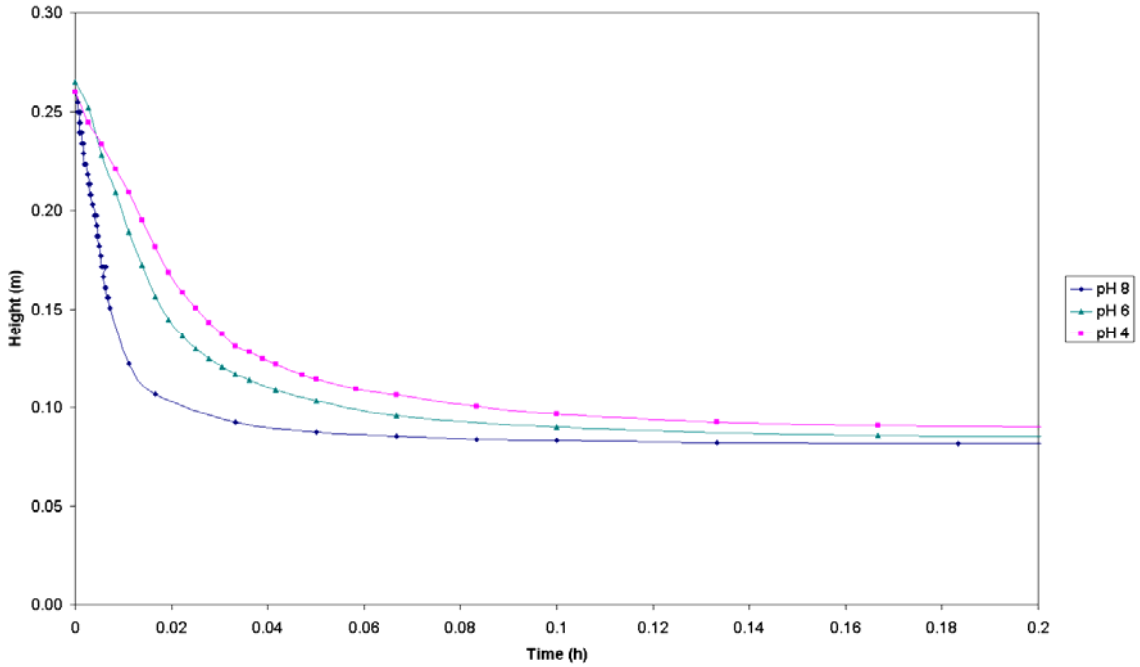


Fig. 4. Settling curves from sediment height as a function of time for 4 wt% kaolinite in 0.01 M NaCl with 0.029 mg/m2 A130 flocculant added at different pH 4, 6, 8.

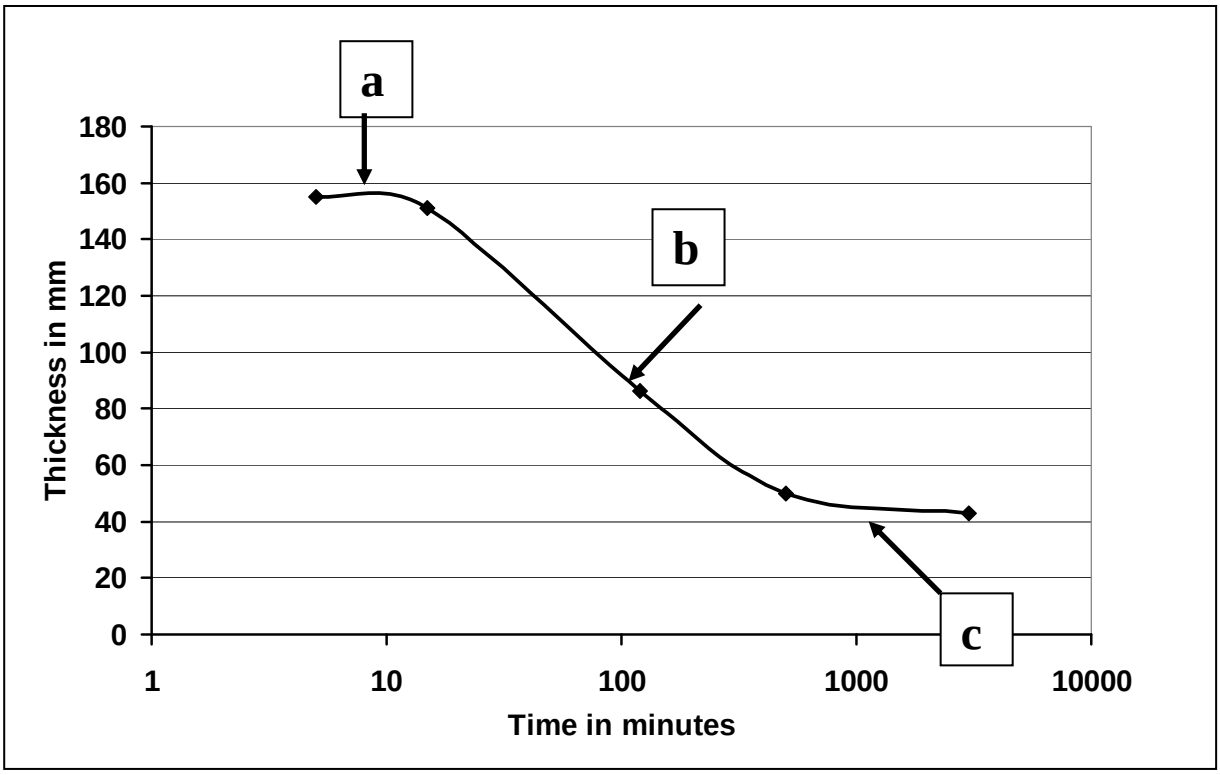


Fig. 5. Settling curve and aggregate structures for 4 wt% Birdwood kaolinite suspension in pH 8 and 0.01 M NaCl or flocculant addition.

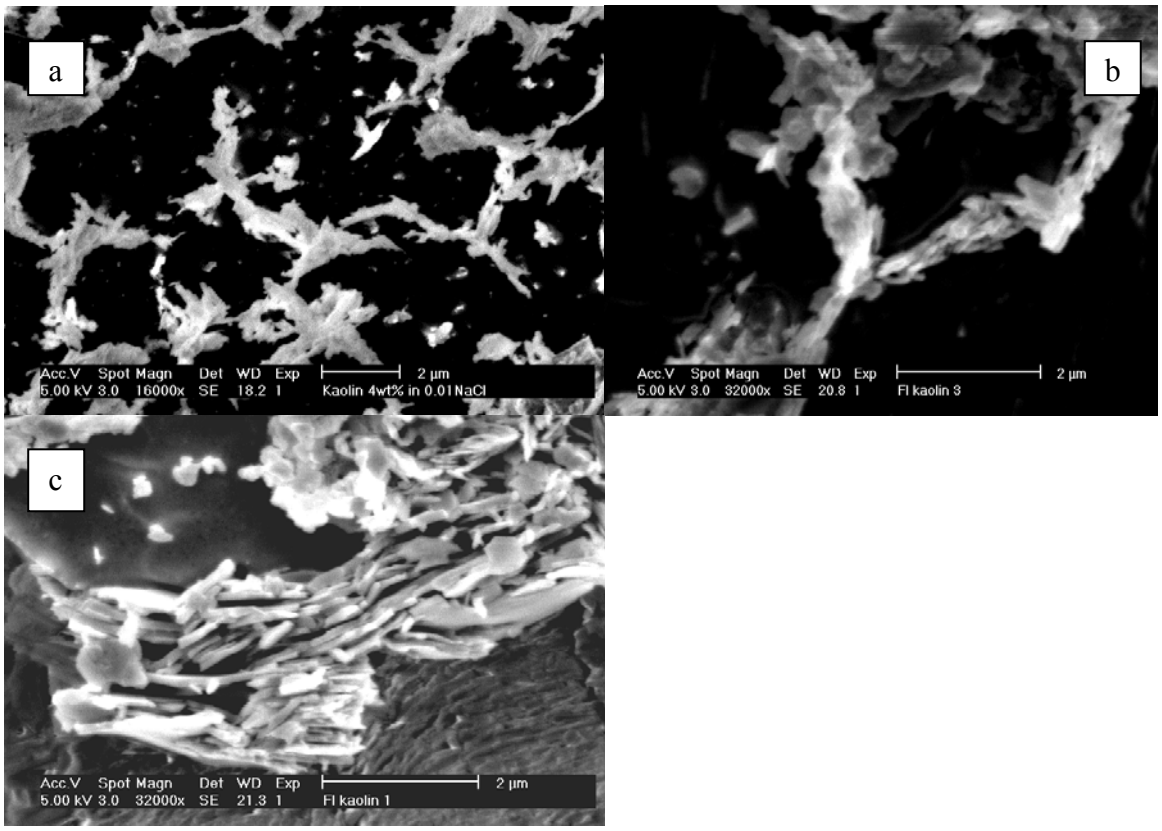


Fig. 6. Enlarged micrographs from Figure 5 corresponding to: (a) first sample-dispersed stage; (b) third stage-pseudo-gelled chain structures; and (c) fourth stage FF-compacted structures.

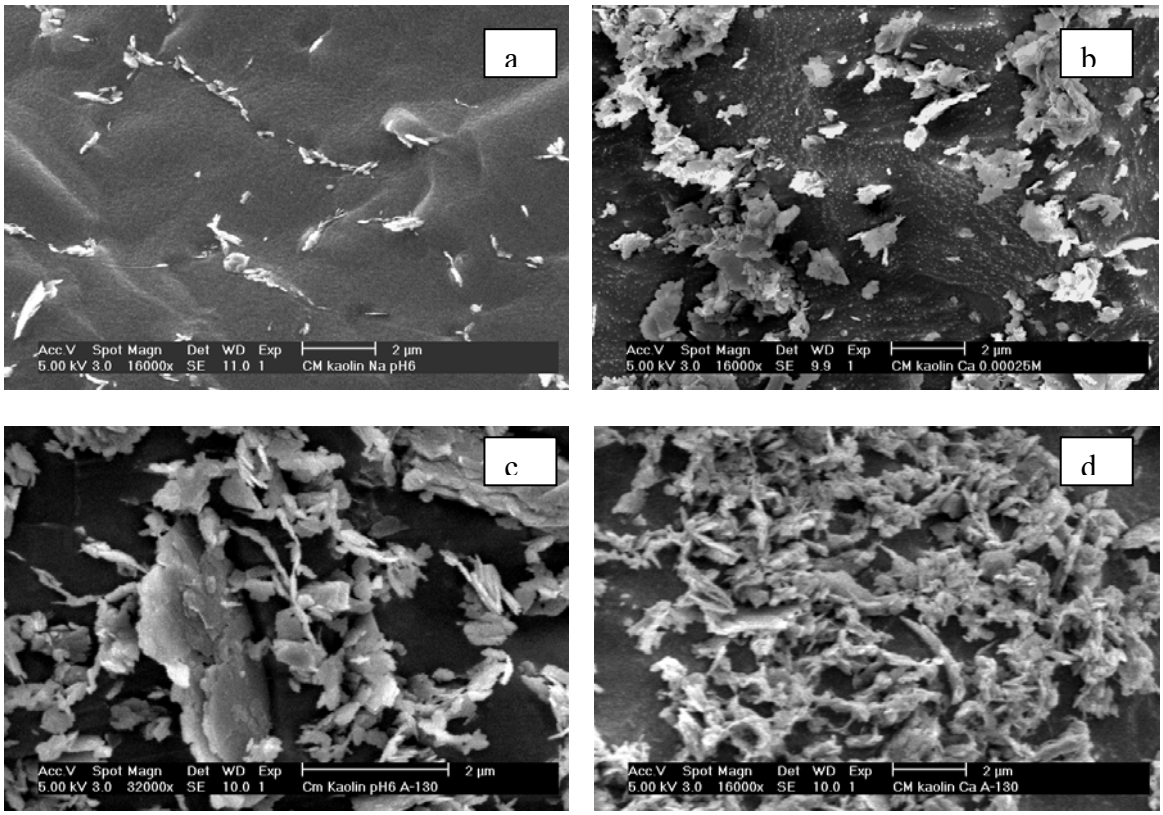


Fig. 7. SEM micrographs from kaolinite suspension without flloculant present (a & b) and with after flocculant (A130) addition (c & d) with Na^{+} and Ca^{2+} ionic solution adjusted to pH 6 sampled near the top of the sediment bed: a, Na; b, Ca; c, Na + A130; d, Ca + A130.

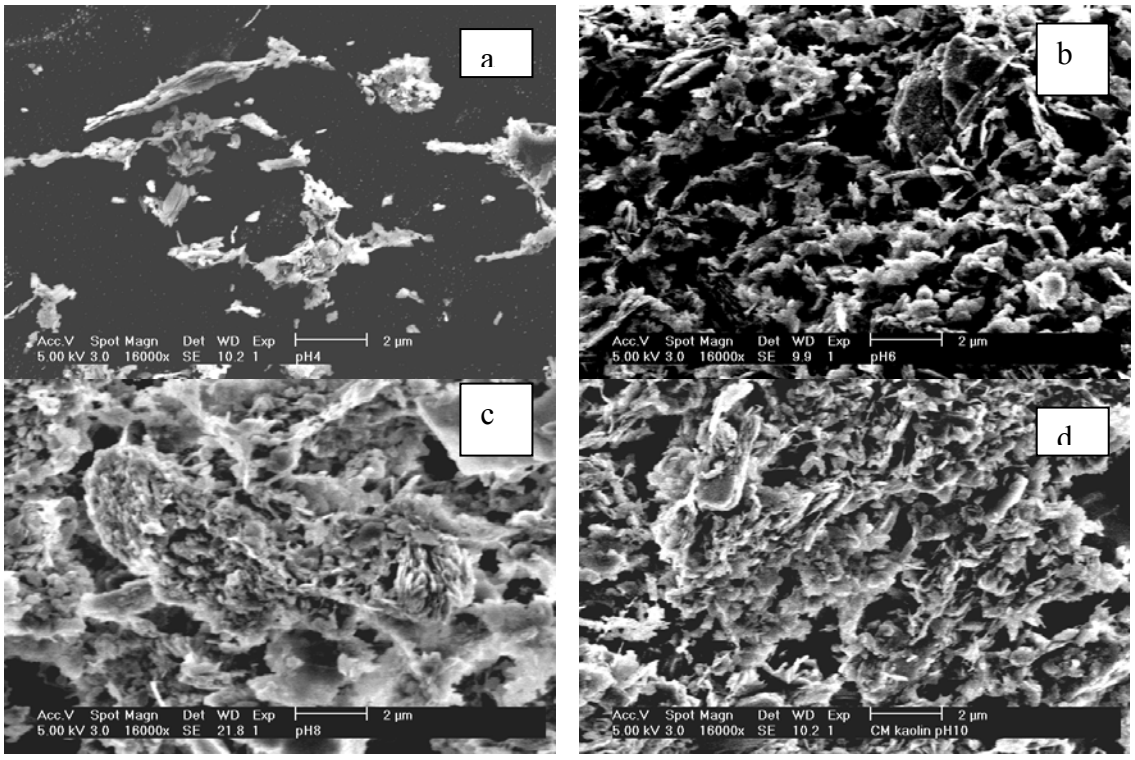


Fig. 8. SEM micrographs from flocculated kaolinite samples with adjustment of pH 8 but sampled near the top of the sediment bed: a, pH 4; b, pH 6; c, pH 8; d, pH 10.

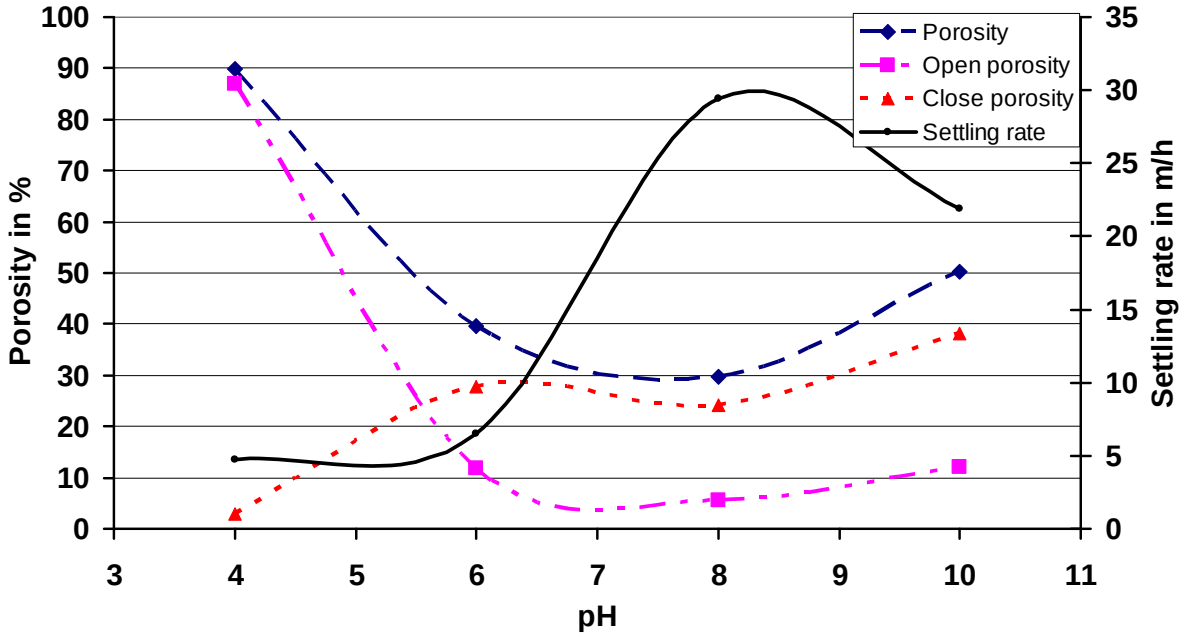


Fig. 9. Porosity analysis from the crio-SEM-STIMAN micrographs, from flocculated kaolinite samples prepared at pH 4, 6, 8, 10 combining images across.

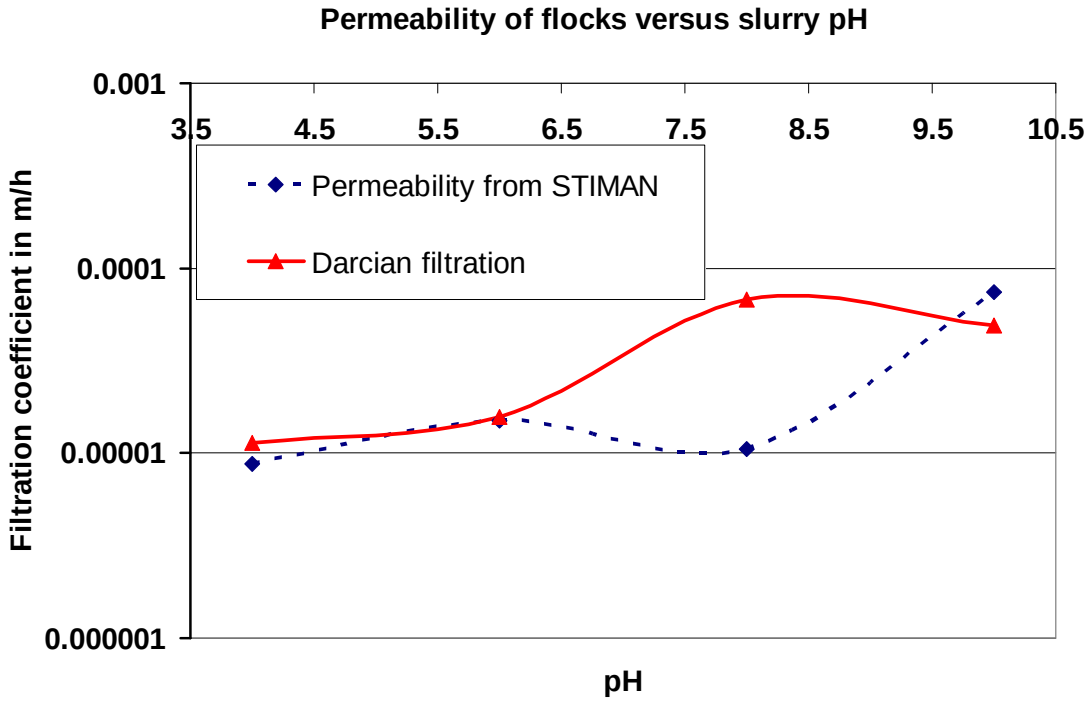


Fig. 10. Permeability values from measured Darcian parameters in equation (2) compared with permeability indices calculated from crio-SEM-STIMAN image analysis from flocculated kaolinite samples.

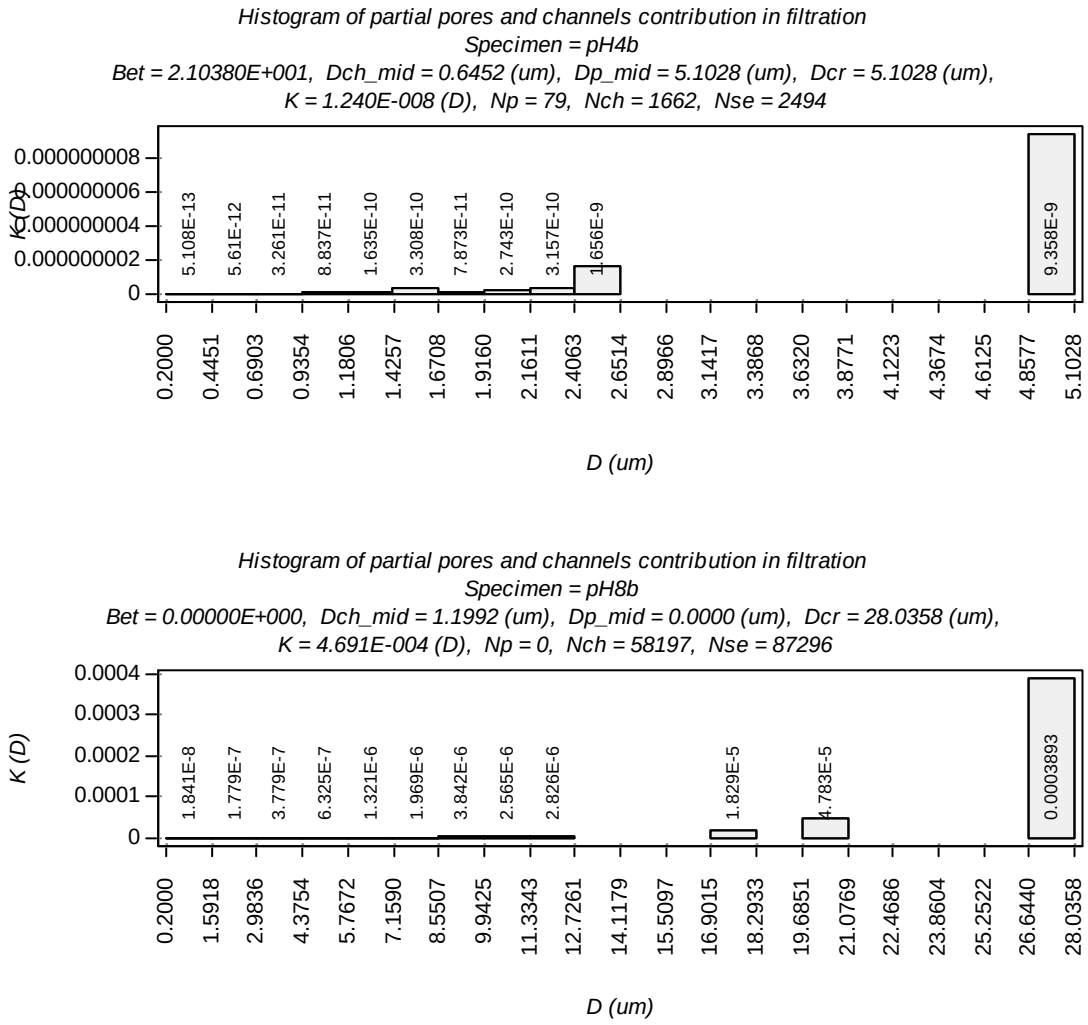


Fig. 11. Histograms of partial pore contributions to total porosity from pH 4 (upper) and pH 8 (lower) micrographs from flocculated kaolinite samples.